Supplementary Information for

# Transport phase diagram and anomalous metallicity in superconducting infinite-layer nickelates

Yu-Te Hsu[*,1,2,3], Kyuho Lee[4,5], Sven Badoux[1,6], Caitlin Duffy[1,6], Alessandro Cuoghi[1], Bai Yang Wang[4,5], Arwin Kool[1], Isaac Haïk-Dunn[6], Harold Y. Hwang[5,7], and Nigel E. Hussey[†,1,8]

[1] *High Field Magnet Laboratory (HFML-FELIX) and Institute for Molecules and Materials, Radboud University, Toernooiveld 7, 6525 ED Nijmegen, Netherlands*

[2] *Department of Physics, National Tsing Hua University, 101, Section 2, Kuang-Fu Road, Hsinchu 300044, Taiwan*

[3] *Department of Materials Science and Engineering, National Tsing Hua University, 101, Section 2, Kuang-Fu Road, Hsinchu 300044, Taiwan*

[4] *Department of Physics, Stanford University, Stanford, CA 94305, United States*

[5] *Stanford Institute for Materials and Energy Sciences, SLAC National Accelerator Laboratory, Menlo Park, Stanford, CA 94025, United States*

[6] *Laboratoire National des Champs Magnétiques Intenses (CNRS, EMFL, INSA, UGA, UPS), Toulouse 31400, France*

[7] *Department of Applied Physics, Stanford University, Stanford, CA 94305, United States*

[8] *H. H. Wills Physics Laboratory, University of Bristol, Tyndall Avenue, Bristol BS8 1TL, United Kingdom*

October 18, 2024

[*] ythsu@phys.nthu.edu.tw

[†] n.e.hussey@bristol.ac.uk

# Supplementary Note A: Analysis of the zero-field resistivity

## A.1. Extraction of characteristic temperatures $T_1$ and $T_2$

$T_1$ and $T_2$ in the zero-field normal state are extracted by two methods: the derivative and linear-fitting method. For the derivative method, $T_1$ corresponds to the lower limit at which $\mathrm{d}\rho_{ab}/\mathrm{d}T$ deviates outside of the noise level set by the data above 250 K; $T_2$ corresponds to the upper limit above which $\mathrm{d}\rho_{ab}/\mathrm{d}(T^2)$ departs from the plateau value set at lower $T$, as illustrated in Supplementary Figs. 1a and 1c. For the linear-fitting method, $\rho_{ab}(T)$ are fitted to $\rho(T) = \rho_0 + A_1 T$ at high $T$ and $\rho(T) = \rho_0 + A_2 T^2$ at low $T$, and divided by the respective fitted curves. $T_1$ and $T_2$ then correspond to the temperature at which $\rho_{ab}/\rho_{\mathrm{fit}}$ deviate more than 1%, as illustrated in Supplementary Fig. 1b. An average of $T_1$ and $T_2$ extracted using the two methods are used to construct Fig. 1 in the main text. The full $\rho_{ab}(T)$ data set measured in zero applied field are shown in Supplementary Fig. 2.
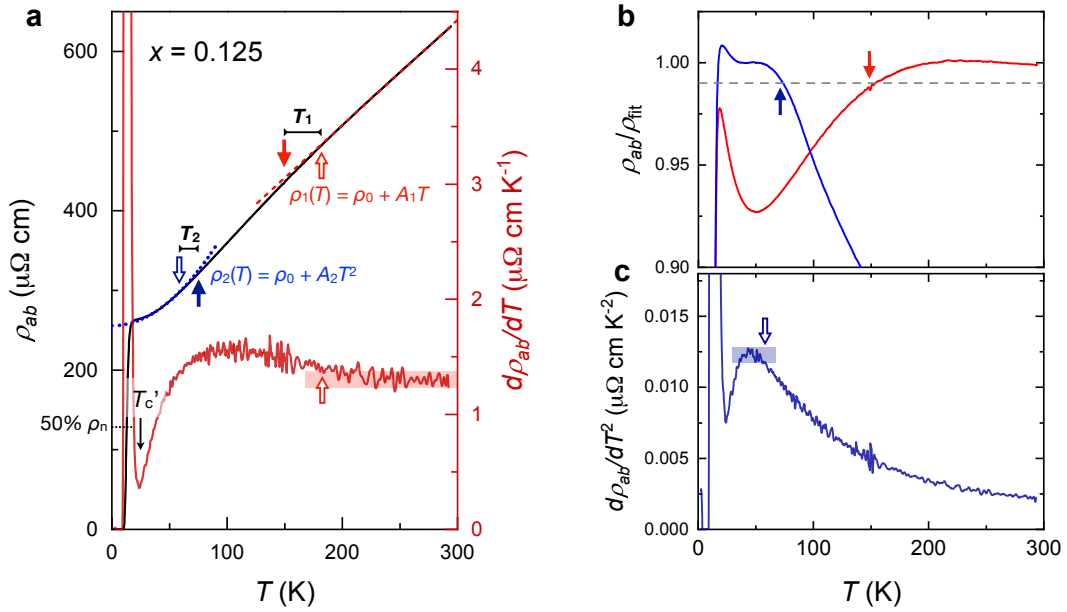


**Supplementary Figure** 1: **Extraction criteria for $T_c$, $T_1$, and $T_2$. a**, Zero-field $T$-dependent in-plane resistivity for $x = 0.125$ (left axis) with the corresponding $T$-derivative (right axis). $T_c'$ corresponds the temperature at which $\mathrm{d}\rho_{ab}/\mathrm{d}T$ shows a steep upturn, which in turn defines the normal-state resistivity value $\rho_n = \rho_{ab}(T_c')$ used for defining $T_c$ and $\mu_0 H_{c2}$. Filled arrows correspond to the characteristic temperature scales $T_1$ (and $T_2$) defined as the temperature at which the measured $\rho_{ab}(T)$ deviates from the $T$-linear fit $\rho_1(T)$ (and $T^2$ fit $\rho_2(T)$) by 1% (panel **b**), respectively; open arrows correspond to the same temperature scales defined by a deviation of $\mathrm{d}\rho_{ab}/\mathrm{d}T$ (and $\mathrm{d}\rho_{ab}/\mathrm{d}(T^2)$) from the plateau values at high $T$ (and low $T$; panel **c**), respectively. An average of the values extracted using the two methods are used for Fig. 1 in the main text. The same method is used to extract $T_1, T_2$, and $T_n$ from $\rho_{ab}(T)$ curves obtained in large magnetic fields.
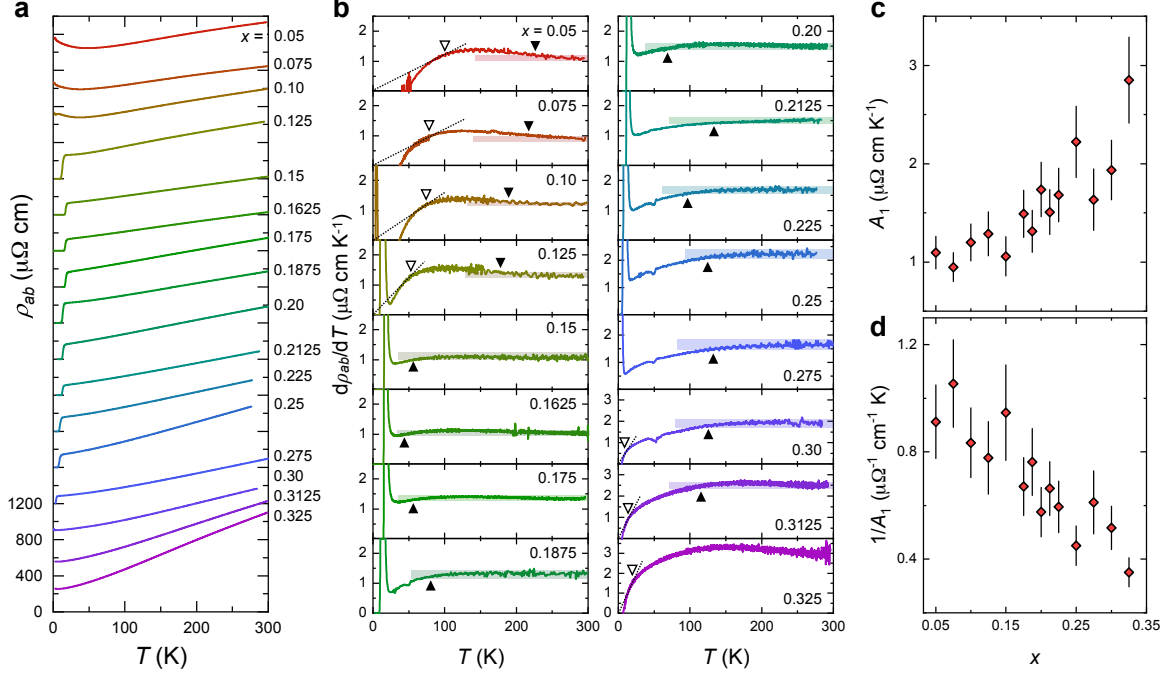
**Supplementary Figure** 2: **Zero-field resistivity of the entire $Nd_{1-x}Sr_xNiO_2$ doping series. a**, Zero-field $\rho_{ab}(T)$ for $0.05 \leqslant x \leqslant 0.325$ and **b**, the corresponding $T$-derivatives. $\rho_{ab}(T)$ traces are shifted vertically by 400 $\mu\Omega$ cm for clarity. $T_0$ is defined as the temperature at which $d\rho_{ab}/dT = 0$ (outside of the superconducting state). The horizontal shaded bars show the $d\rho_{ab}/dT$ at the high-$T$ plateaus with the noise levels. Filled (open) triangles are the corresponding $T_1$ $(T_2)$ values extracted using the derivative method, respectively. Note that the dips at around 50 K in some of the $d\rho_{ab}/dT$ curves are experimental artefacts due to thermometer calibration of the commercial measurement system (PPMS by Quantum Design Inc.) used. For $x = 0.325$ (and $x = 0.3125$ to a lesser extent), the gradual increase in $d\rho_{ab}/dT$ with decreasing $T$ below 250 K (which may be due to the higher level of disorder as reflected by the larger residual resistivity) makes it difficult to reliably extract $T_1$ using the derivative method, though we could still estimate its $A_1$ from $d\rho_{ab}/dT$ above 250 K. **c**, Slope of $T$-linear resistivity at high temperatures $A_1$ versus $x$ and **d**, the inverse of $A_1$ versus $x$. $1/A_1$ decreases approximately linearly with increasing $x$, contrasting to that found in the hole-doped cuprates[1] and possibly suggesting a reduction of electronic density of states at the Fermi level with increasing $x$. The error bars in $A_1$ and $1/A_1$, assumed to be 15%, correspond to the geometric uncertainties of measured samples.

## A.2. Quantitative evaluation of in-plane resistivity

The largest contributor to the uncertainty in determining the in-plane resistivity values in our films is the determination of effective film thickness. Given the films have a total thickness of roughly 15 unit cells, a sharp step in the substrate would lead thickness variation of 1-2 unit cells, which translates to an uncertainty in thickness within 7–14%. In previous work conducted on the same set of samples,[2] we have demonstrated that the high-$T$ $d\rho_{ab}/dT$ in NSNO and LSCO near respective optimal doping have nearly identical magnitudes ($\approx 1.1$ $\mu\Omega$ cm K$^{-1}$). The fact that the absolute values of $d\rho_{ab}/dT$ between these two systems show striking similarity suggests that level of residual disorder does not play a dominant role in determining the prefactor of $T$-dependent resistivity. We also note that $d\rho_{ab}/dT$ at high $T$ for films with $0.15 \leqslant x \leqslant 0.30$ increases with $x$ (Supplementary Fig. 2c), meanwhile $\rho_0$ decreases slightly as $x$ increases in this doping range. This observation shows that the magnitude of $T$-dependent resistivity is not dictated by residual resistivity of our films, and the findings reported here on charge transport in NSNO thin films is not significantly impacted by the level of excess disorder.

## A.3. Comparison with LSCO

The fan of $T$-linear resistivity that spans the NSNO phase diagram – depicted in Fig. 1 of the main article – is highly reminiscent of the fan previously reported in LSCO.[3] In the latter, this fan has been interpreted as emerging from a singular QCP near the doping level $p^*$ at which the pseudogap phase closes.[4] The expectation within such a picture is that a FL ground state is restored at sufficiently low temperatures with $\rho(T) \propto T^2$ with a coefficient that grows (diverges) as $p \to p^*$. High-field transport studies, however, indicate that in contrast to expectations, $\rho_{ab}(T)$ in overdoped LSCO retains a dominant $T$-linear component down to the lowest temperatures, with a coefficient $\alpha_1(0)$ that dropped monotonically with increasing $p$,[5] while the sub-dominant $T^2$ term shows very little change with doping.

The presence of a small resistive upturn in our NSNO films beyond $x_{\mathrm{opt}}$ makes it difficult to identify a pure $T$-linear component in $\rho_{ab}(T)$ (finite intercept in $d\rho_{ab}/dT$) at low-$T$, and as discussed in the main text, the $T$-dependence is best described by a single power-law with a non-integer exponent. Nevertheless, given the similarities in the form of $\rho_{ab}(T)$ at higher temperatures, it is perhaps prudent to examine whether or not we can rule out a similar evolution in the form of $\rho_{ab}(T)$ ($d\rho_{ab}/dT$) in NSNO to that observed in LSCO.

The high-$T$ coefficient $\alpha_1(\infty)$ is extracted directly from the $d\rho_{ab}/dT$ curves plotted in Supplementary Fig. 2. To obtain $\alpha_1(0)$, we performed a linear extrapolation of the intermediate-$T$ slopes of $d\rho_{ab}/dT$ down to 0 K and read off the intercept. This process inevitably invokes a

larger uncertainty, but we note that uncertainty in the absolute values of $\rho_{ab}(T)$ – notoriously difficult to determine precisely in such thin films – is removed by taking the ratio of the two coefficients.

The result of this exercise is shown in Supplementary Fig. 3. The blue squares are taken directly from ref.[3] The agreement between the two data sets is indeed striking. While this analysis does not confirm that $\rho_{ab}(T) = \alpha_0 + \alpha_1(0)T + \alpha_2 T^2$ in NSNO at low $T$, it is important to acknowledge that this possible link does exist.
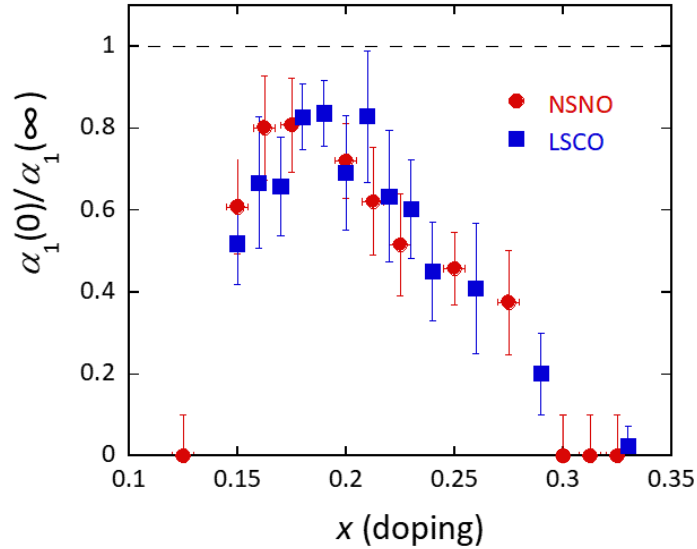


**Supplementary Figure** 3: **Comparison of $T$-linear coefficients in NSNO and LSCO.** Doping dependence of the ratio $\alpha_1(0)/\alpha_1(\infty)$ as a function of Sr concentration in NSNO (red circles) and LSCO (blue suqares). Here, $\alpha_1(\infty)$ is the coefficient of the high-$T$ $T$-linear resistivity and $\alpha_1(0)$ is the corresponding low-$T$ $T$-linear coefficient obtained by linearly extrapolating the intermediate-$T$ slopes of $d\rho_{ab}/dT$ shown in Supplementary Fig. 2 down to 0 K. The error bars correspond to the uncertainty in extrapolated $\alpha_1(0)$ values by fitting the low-$T$ resistivity data.

**Supplementary Note B: Form of normal-state MR near $x_{\mathrm{opt}}$**

The validity of established MR functional forms in describing the normal-state MR in NSNO is critically examined. Supplementary Fig. 4 illustrates the violation of Kohler's scaling $(\Delta\rho(H)/\rho(0) \propto H/\rho(0))$, known to be successful to capture the orbital MR in conventional metals, and quadrature scaling $\Delta\rho(H)/T \propto H/T$, recently found to be valid in hole-doped cuprates as well as several quantum critical metals. We further examine whether the $T = 25$ K MR traces for $x \approx x_{\mathrm{opt}}$ can be fitted to a conventional two-carrier model or other empirical models, as shown in Supplementary Fig. 5. While all the trial models can fit the 25-K data

reasonably well, we find that the power-law fit $\Delta\rho(H) \propto H^m$ shows highest $R^2$ and lowest $\chi^2$ values, demonstrating a quantitative superiority of the power-law function in describing the normal-state MR in NSNO.
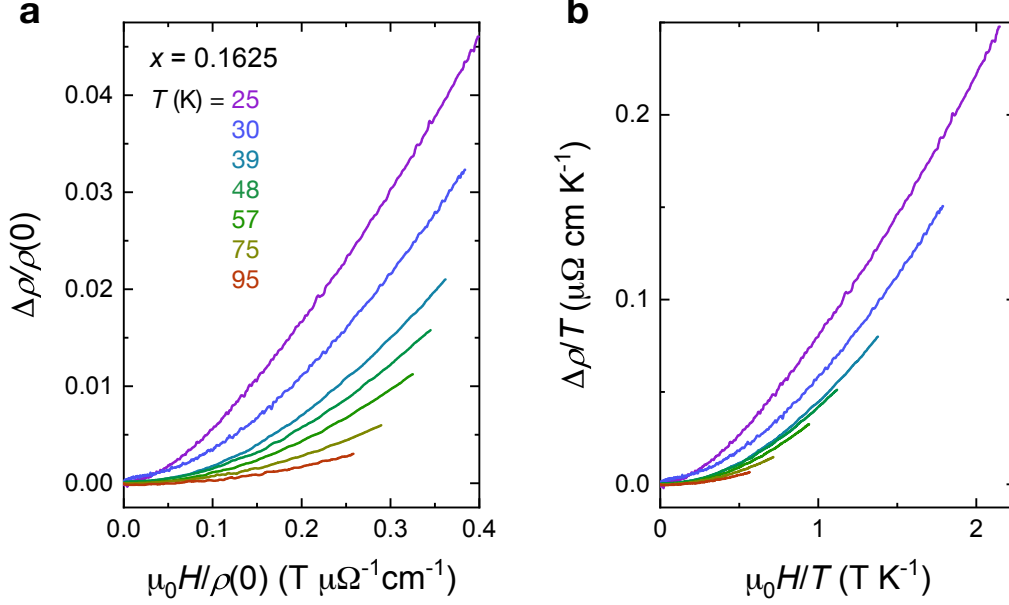


**Supplementary Figure** 4: **Absence of scaling collapse in the normal-state MR for** $x = 0.1625$. **a**, $\Delta\rho/\rho(0)$ versus $\mu_0 H/\rho(0)$, known as the Kohler's plot, for $T > T_c$. **b**, $\Delta\rho/T$ versus $\mu_0 H/T$, which will lead to a scaling collapse if $\Delta\rho(H,T) \propto \sqrt{(\alpha k_B T)^2 + (\gamma \mu_B \mu_0 H)^2}$. No scaling of either kind is found for $Nd_{1-x}Sr_xNiO_2$ at $x = 0.1625$.

To inspect the MR evolution below $T_c$, we first have to identify the field scale at which the normal-state behaviour is recovered. As the field-derivative of magnetoresistivity always increases with field (i.e. $d^2\rho_{ab}/d(H^2) > 0$) at $T > T_c$, we use the manifestation of a positive slope in $d\rho_{ab}/dH$ as indicative of the normal-state recovery, and fitted the MR data below $T_c$ using the power-law expression (as well as the other two functions trialed in Supplementary Fig. 5), as shown in Supplementary Fig. 6-9. We find that the extrapolated zero-field resistivity below $T_c$, regardless of the fitting function, does not follow a pure $T$-linear behaviour as $T \to 0$ (Supplementary Fig. 6-8). Furthermore, we find that the MR slope ($d\rho_{ab}/d\mu_0 H$) increases by more than one order of magnitude as $T$ decreases from 95 to 1.4 K (Supplementary Fig. 10a), whereas $d\rho_{ab}/d\mu_0 H$ at a constant $T = 25$ K does not correlate with the zero-field resistivity (Supplementary Fig. 10b), indicating the MR magnitude is not set by the level of disorder itself but controlled by the level of Sr doping.
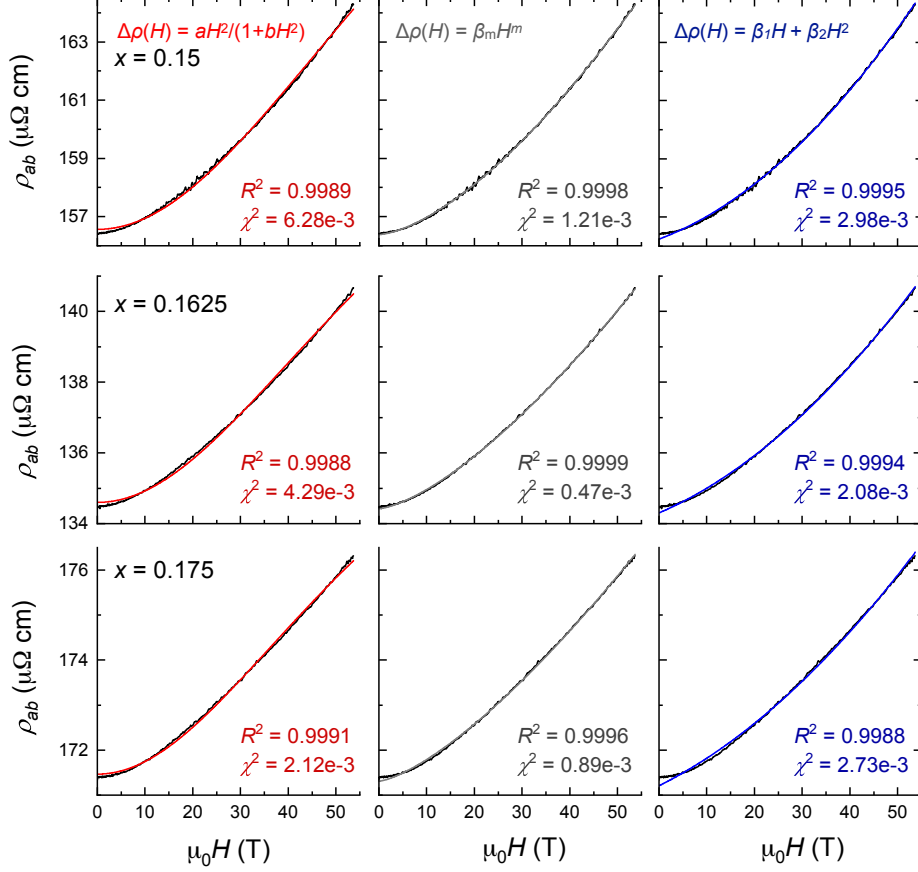
**Supplementary Figure** 5: **Comparison of model fitness to measured magneto-resistivity in nearly optimally doped films.** $\rho_{ab}(H)$ traces measured at 25 K for each sample ($x = 0.15$, top row; $x = 0.165$, middle row; $x = 0.175$, bottom row) are fitted to an empirical two-carrier function (left column), a power-law function (middle column), and a dual-component function (right column). The 25-K MR trace is used as it is closest to the zero-field $T_c'$ values for these films, which allows us to access the normal state over the widest field range. The corresponding $R^2$ and reduced $\chi^2$ values of the fits are specified. The power-law function consistently yields the highest $R^2$ and lowest $\chi^2$ for all $x \approx x_{\text{opt}}$, indicating a statistical superiority of the power-law function in describing the normal-state MR.
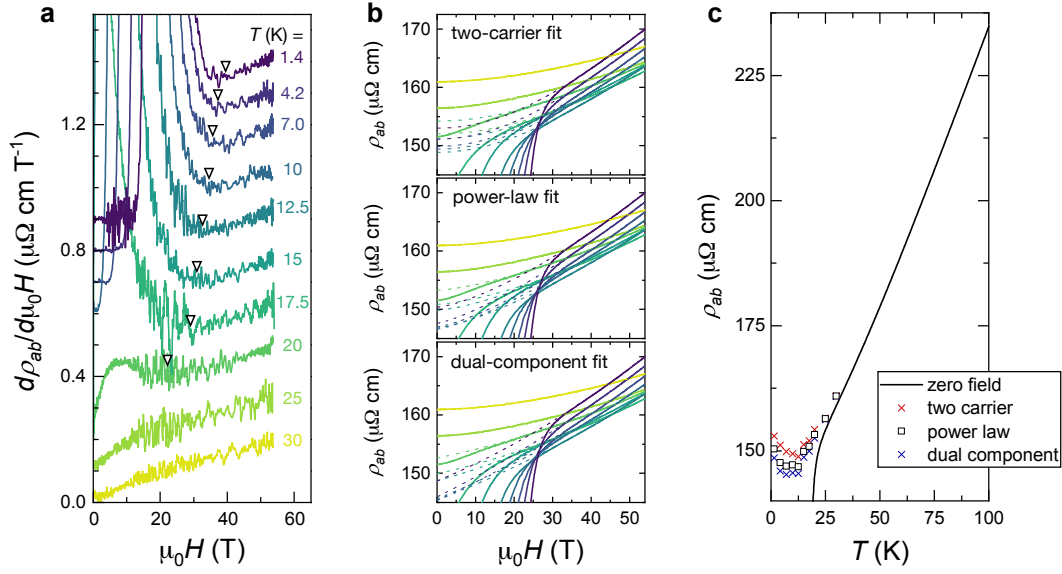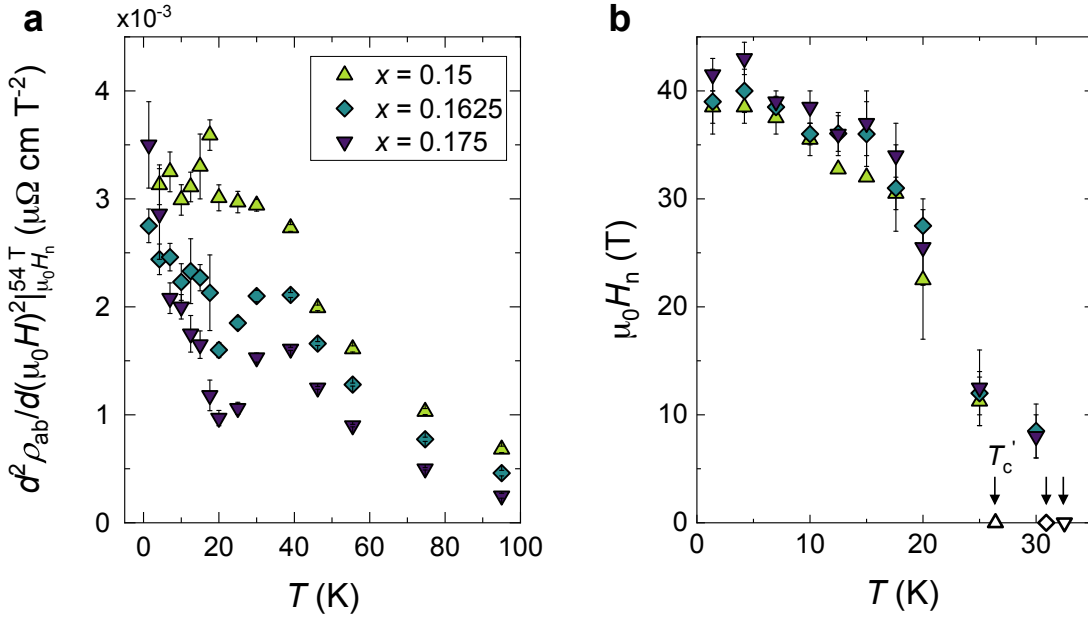
**Supplementary Figure** 6: **Field range of normal-state MR and extrapolation of zero-field resistivity for** $x = 0.15$**. a**, $\mathrm{d}\rho_{ab}/\mathrm{d}\mu_0 H$ below 30 K. Each trace is vertically shifted by 0.1 $\mu\Omega$ cm $\mathrm{T}^{-1}$ for clarity. (Recall that in Fig. 3a of the main article, these $\mathrm{d}\rho_{ab}/\mathrm{d}\mu_0 H$ curves were not vertically shifted.) Open triangles indicate the field strength $(H_\mathrm{n})$ above which the normal-state behaviour is recovered. **b**, Fits made to $\rho_{ab}(H)$ isotherms at $H \geqslant H_\mathrm{n}$, shown in dashed lines, using $\rho(H) = \rho(0) + AH^2/(1 + BH^2)$ (top), $\rho(H) = \rho(0) + \beta_m H^m$ (middle), and $\rho(H) = \rho(0) + \beta_1 H + \beta_2 H^2$ (bottom), respectively. **c**, Extracted zero-field resistivity $\rho_{ab}(T, H = 0)$ using each of the trial functions. Very similar behaviour is found irrespective of the fitting function.
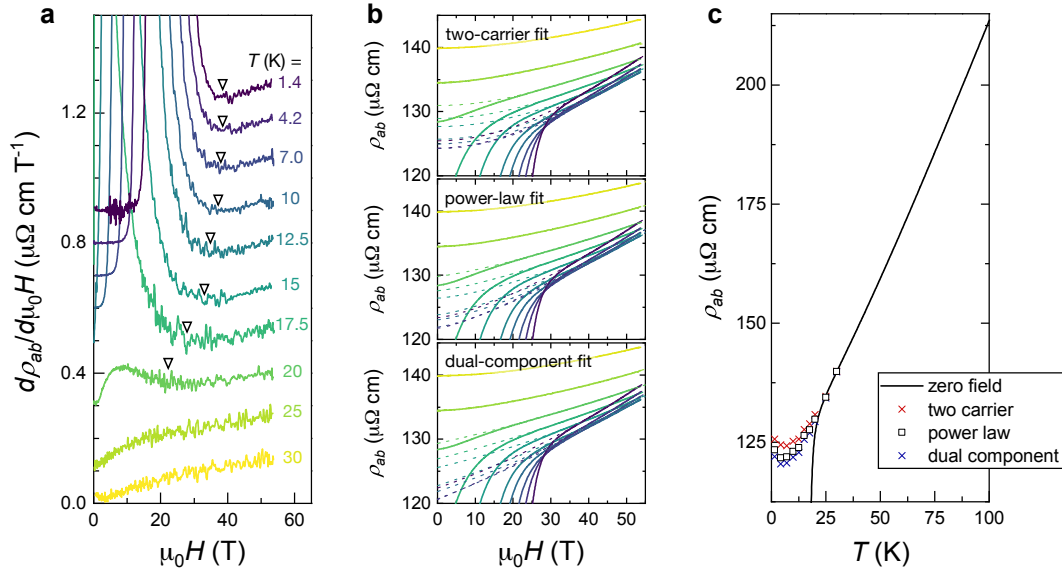


**Supplementary Figure** 7: **Field range of normal-state MR and extrapolation of zero-field resistivity for** $x = 0.1625$**.** The same figure as Supplementary Fig. 6 with $x = 0.1625$.

8
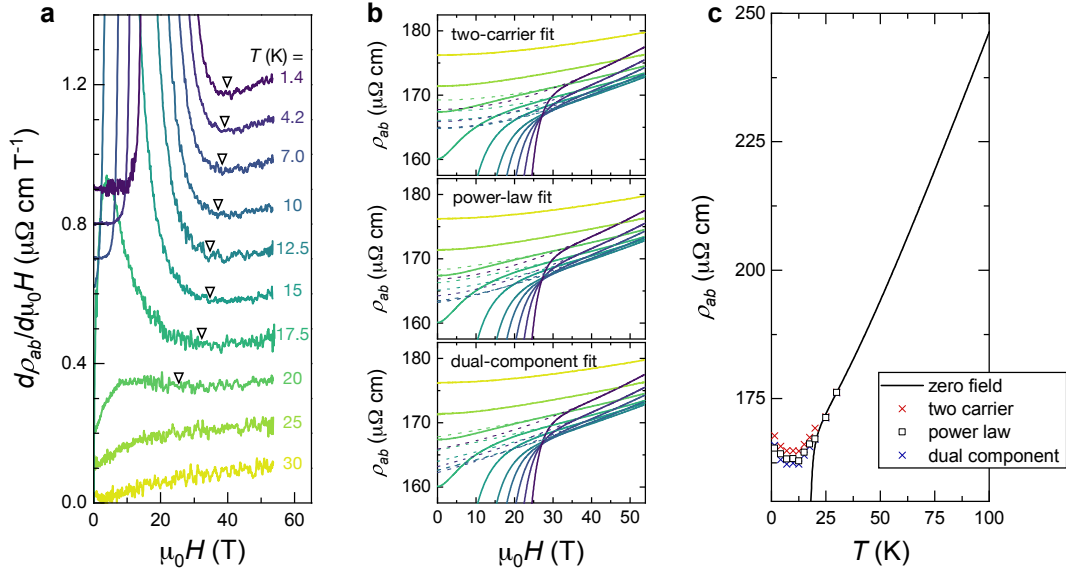
**Supplementary Figure** 8: **Field range of normal-state MR and extrapolation of zero-field resistivity for** $x = 0.175$. The same figure as Supplementary Fig. 6 with $x = 0.175$.



**Supplementary Figure** 9: **Normal-state MR slopes and field scale for** $x \approx x_{\mathrm{opt}}$. **a**, The slope of $\mathrm{d}\rho_{ab}/\mathrm{d}\mu_0 H$ between $\mu_0 H_n$ and 54 T and **b**, the magnetic field scale $\mu_0 H_n$ above which the normal-state behaviour is recovered, as a function of temperature $T$. The error bars in $\mathrm{d}\rho_{ab}/\mathrm{d}\mu_0 H$ reflect the uncertainty in the linear fits to the normal-state data between $\mu_0 H_n$ and 54 T.
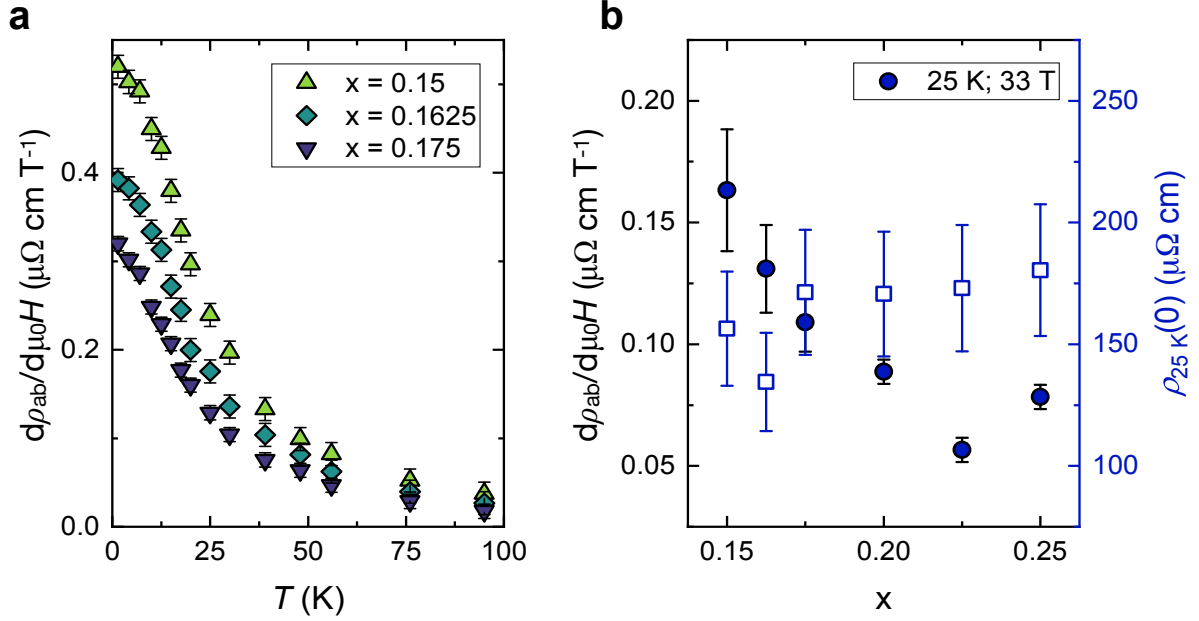
**Supplementary Figure** 10: **Temperature and doping evolution of high-field MR slopes. a**, MR slope at 53 T for $x$ near $x_{\mathrm{opt}}$ over wide temperature range 1.4 K $\leqslant$ $T \leqslant$ 95 K. An order-of-magnitude increase in differential MR $\mathrm{d}\rho_{ab}/\mathrm{d}\mu_0 H$ is observed between 1.4 and 95 K. **b**, MR slope at 33 T (left axis) and zero-field resistivity at 25 K (right axis) for $0.15 \leqslant x \leqslant 0.25$. The error bars in $A_1$ and $1/A_1$, assumed to be 15%, correspond to the geometric uncertainties of measured samples. An overall suppression in $\mathrm{d}\rho_{ab}/\mathrm{d}\mu_0 H$ with increasing $x$ is found, while $\rho_{25\ \mathrm{K}}(0)$ remains largely unchanged with respect to $x$.

## Supplementary Note C: Details of Boltzmann MR simulations

Within a Boltzmann theoretical framework, the rapid increase in MR magnitude with decreasing $T$ can only be reconciled by invoking a corresponding and marked increase in the $k$-space anisotropy of the mean-free-path $\ell$ (under the assumption that there is no change in the carrier density across $T = T_0$). Such a circumstance, coupled with Fermi surface regions of differing curvature, was invoked previously to explain the $T$- and $x$-dependence of the Hall coefficient $R_{\mathrm{H}}(T)$ in overdoped LSCO.[6,7] Intriguingly, $R_{\mathrm{H}}(T)$ in near-optimally-doped NSNO also exhibits a similar $T$-dependence to that observed in overdoped LSCO.[2,8] This correspondence supports the notion that the MR response in NSNO can be qualitatively understood in terms of strong anisotropy in the elastic scattering channel (i.e., the impurity-limited mean-free-path $\ell$) that is gradually smeared out with increasing $H$ (due to the ever-increasing cyclotron motion) and increasing $T$ (due to the growth of an inelastic scattering rate that is effectively isotropic in $k$-space). We note that this simulation only serves as an illustration that an unconventional power-law MR can be qualitatively captured using an approximate Fermi surface parametrisation with certain models of anistropic scatterings. Clearly, future studies of the Hall response up to comparable field strengths will confirm whether this picture can capture the full magnetotransport response in NSNO.

## Supplementary Note D: Extrapolations of zero-field resistivity below $T_{\mathrm{c}}$ in overdoped NSNO
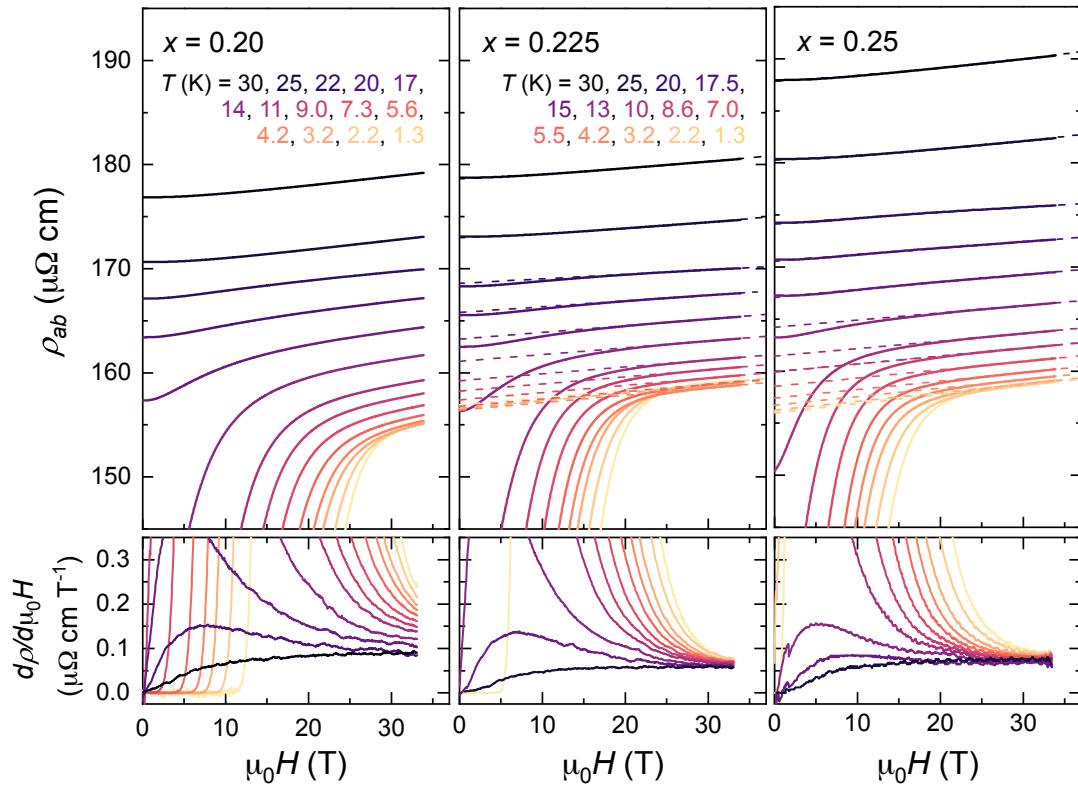
Supplementary Fig. 12 shows magnetoresistivity traces measured at $T \leqslant 30$ K in overdoped NSNO with $0.20 \leqslant x \leqslant 0.25$. For $x = 0.225$ and 0.25, we estimate the zero-field normal-state resistivity below $T_{\mathrm{c}}$ by fitting the (nearly) normal-state MR using the dual-component expression: $\rho(H) = \rho(0) + \beta_1 H + \beta_2 H^2$, as the narrow field range of normal-state behaviour prevents a reliable extraction of $\rho_{ab}(T, H = 0)$ using the single power-law expression. For $x = 0.20$, the normal-state MR cannot be accessed below 34 T for $T \lesssim 10$ K.
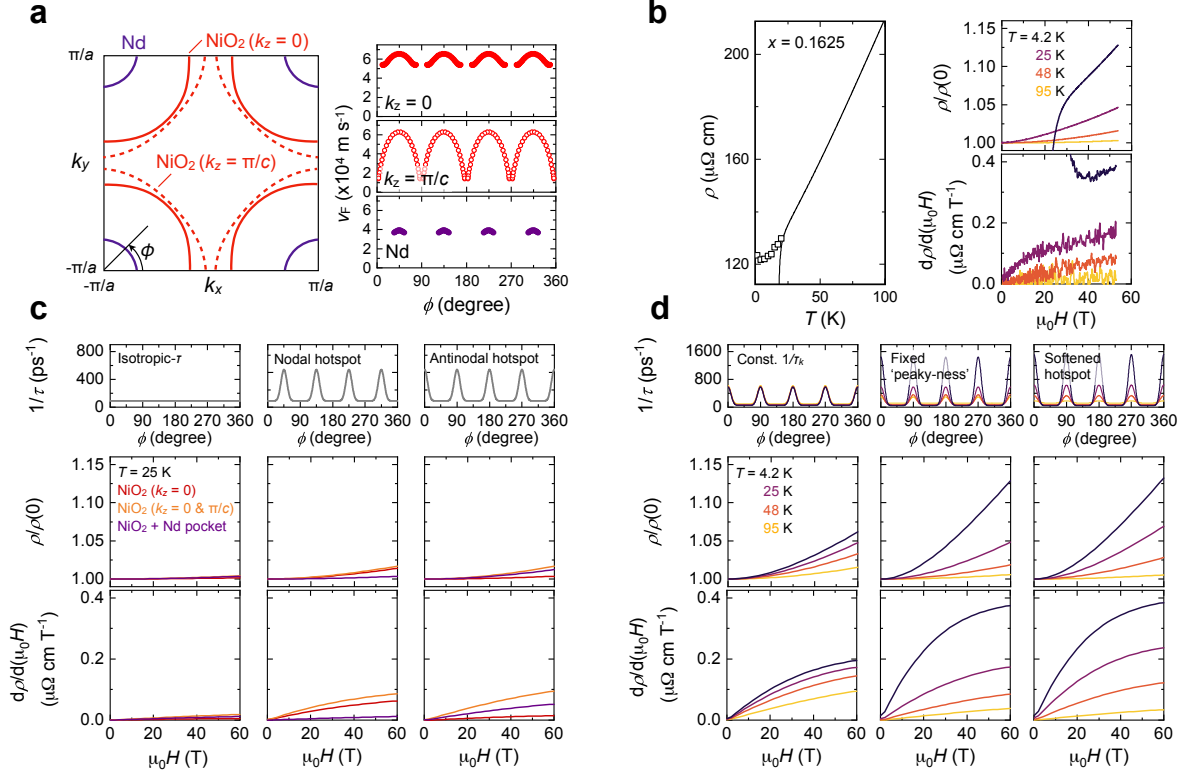
**Supplementary Figure** 11: **Simulations of MR in superconducting nickelates using Boltzmann transport formalism with $k$-dependent anisotropic scattering. a**, Fermi surface parameterisation of NSNO near optimal doping. Solid and dashed red lines correspond to Ni $d_{x^2-y^2}$ band at $k_z = 0$ and $k_z = \pi/c$, respectively, and purple line corresponds to the Nd pocket. All electronic bands are derived from the tight-binding model developed in ref.[9] Corresponding Fermi velocity $v_F$ as a function of azimuthal angle $\phi$ are shown on the right panels. **b**, Experimental MR data measured on NSNO ($x = 0.1625$). Zero-field resistivity and $d\rho_{ab}/dH$ values at selected temperatures are used as benchmarks for consistency check of simulated results. **c**, Effect of Fermi surface parameterisation and scattering anisotropy on simulated MR at $T = 25$ K. The inclusion of two Ni sheets increases the simulated MR in all scattering anisotropy scenarios considered, whereas the inclusion of Nd pocket decreases the MR magnitude. The antinodal hotspot scenario ($\tau^{-1} = \tau_0^{-1} + \tau_k^{-1}|\cos(2\phi)|^\nu$) produces a simulated $d\rho_{ab}/dH$ closest to the experimental $d\rho_{ab}/dH$ at 25 K. **d**, MR simulations at selected temperatures with different forms of antinodal hotspot parametrisation, using a two Ni-sheet Fermi surface. For the constant $1/\tau_k$ scenario, a $T$-independent $1/\tau_k(= 523$ ps$^{-1}$) and $\nu = 12$ is used with $1/\tau_0$ tuned to match the zero-field resistivity $\rho(0)$ to experimental values within 1 $\mu\Omega$ cm. For the fixed 'peaky-ness' scenario, a $T$-independent $\nu$ is used with $\tau_k/\tau_0$ and $\tau_0^{-1}$ tuned to match the experimental $d\rho_{ab}/dH$ at 54 T and $\rho(0)$ at each $T$, respectively. For the softened hotspot scenario, a trial set of $\nu = (12, 10, 8, 4)$ is used at $T = (4.2, 25, 48, 95)$ K with $\tau_k/\tau_0$ and $\tau_0^{-1}$ tuned to match the experimental $d\rho_{ab}/dH$ at 54 T and $\rho(0)$ at each $T$, respectively. Parameters used to generate the simulated results are shown in Table 1.

**Supplementary Table** 1: **Parameters used for MR simulations within scenarios considered.** Isotropic-$\tau$: $1/\tau = 1/\tau_0$; nodal hotspot: $1/\tau = 1/\tau_0 + 1/\tau_k|\sin(2\phi)|^\nu$; antinodal hotspot: $1/\tau = 1/\tau_0 + 1/\tau_k|\cos(2\phi)|^\nu$. I, II, III corresponds to the Fermi surface parameterisation using a single Ni Fermi sheet ($k_z = 0$), two Ni Fermi sheets ($k_z = 0$ and $\pi/c$), and two Ni Fermi sheets plus Nd pocket, respectively. For the $T$-dependent simulations, the two-Ni-Fermi-sheet scenario is used for Fermi surface parametrisation.

| Scenario | $T$ (K) | $\rho(0)(\mu\Omega$ cm$)$ | $1/\tau_0$ (ps$^{-1}$) | $1/\tau_k$ (ps$^{-1}$) | $\nu$ |
|---|---|---|---|---|---|
| Experiment | 25 | 134.4 | - | - | - |
| Isotropic-$\tau$ (I) | 25 | 121.1 | 90 | 0 | - |
| Isotropic-$\tau$ (II) | 25 | 138.4 | 90 | 0 | - |
| Isotropic-$\tau$ (III) | 25 | 110.2 | 90 | 0 | - |
| Nodal hotspot (I) | 25 | 159.3 | 90 | 450 | 12 |
| Nodal hotspot (II) | 25 | 185.8 | 90 | 450 | 12 |
| Nodal hotspot (III) | 25 | 138.2 | 90 | 450 | 12 |
| Antinodal hotspot (I) | 25 | 163.0 | 90 | 450 | 12 |
| Antinodal hotspot (II) | 25 | 190.2 | 90 | 450 | 12 |
| Antinodal hotspot (III) | 25 | 140.6 | 90 | 450 | 12 |
| Constant $1/\tau_k$ | 4.2 | 121.5 | 51.2 | 523 | 12 |
|  | 25 | 135.1 | 58.1 | 523 | 12 |
|  | 48 | 155.5 | 68.8 | 523 | 12 |
|  | 95 | 207.5 | 97.0 | 523 | 12 |
| Fixed peaky-ness | 4.2 | 121.6 | 42.3 | 1400 | 12 |
|  | 25 | 134.4 | 57.7 | 525 | 12 |
|  | 48 | 155.9 | 77.5 | 280 | 12 |
|  | 95 | 207.6 | 115 | 180 | 12 |
| Softened hotspot | 4.2 | 122.0 | 42.1 | 1470 | 12 |
|  | 25 | 134.0 | 52.1 | 585 | 10 |
|  | 48 | 156.1 | 69.8 | 262 | 8 |
|  | 95 | 207.5 | 113 | 70.7 | 4 |

**Supplementary Figure** 12: **Magnetoresistivity isotherms and corresponding field-derivatives for** $x = 0.20, 0.225$ **and** $0.25$ **films.** The same colour coding is shared by $x = 0.225$ and $0.25$.

## Supplementary Note E: Form of low-$T$ normal-state resistivity

In Supplementary Figs. 13 and 14 we examine the validity of three expressions to describe the low-$T$ normal-state resistivity in OD-NSNO: a purely $T^2$ resistivity ($\Delta\rho(T) = A_2 T^2$), a dual-component resistivity ($\Delta\rho(T) = \alpha_1 T + \alpha_2 T^2$), and a power-law resistivity ($\Delta\rho(T) = \alpha_n T^n$). As discussed in the main text, a purely $T^2$ resistivity is only valid within a narrow $T$ window, especially for $x = 0.275$ in which the normal-state resistivity can be accessed over the widest $T$ window. Comparing the two alternative cases, the power-law expression is consistently valid over a wider $T$ window for all $x$ (Supplementary Figs. 13 and 14d). Therefore, we conclude that a single power-law resistivity $\Delta\rho(T) = \alpha_n T^n$ with $n \approx 1.5$ provides the best description for the low-$T$ normal-state resistivity in OD-NSNO.
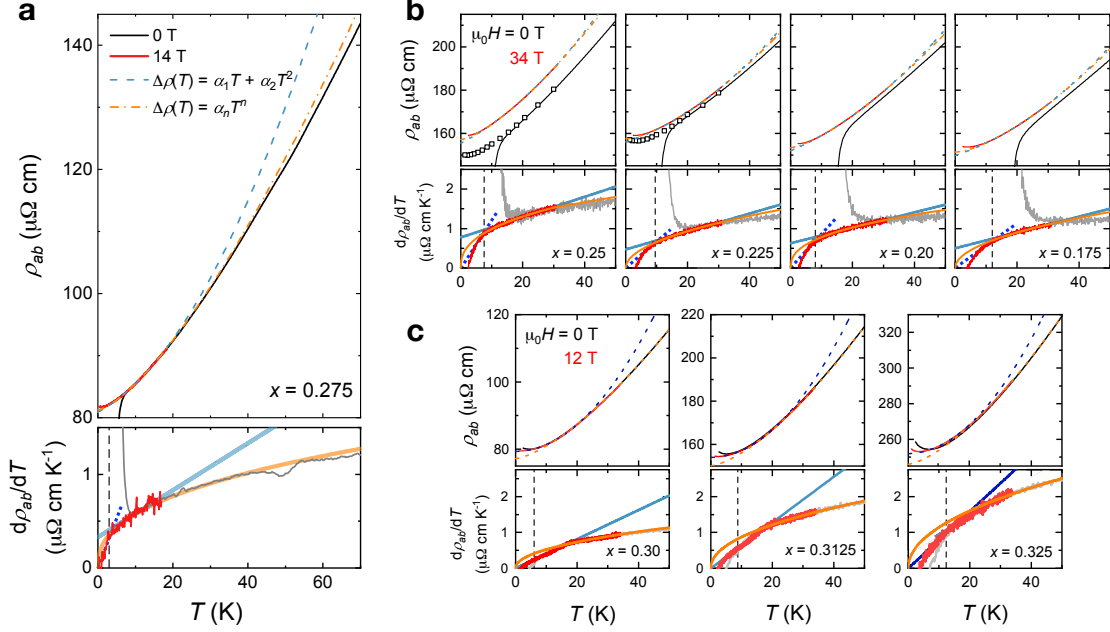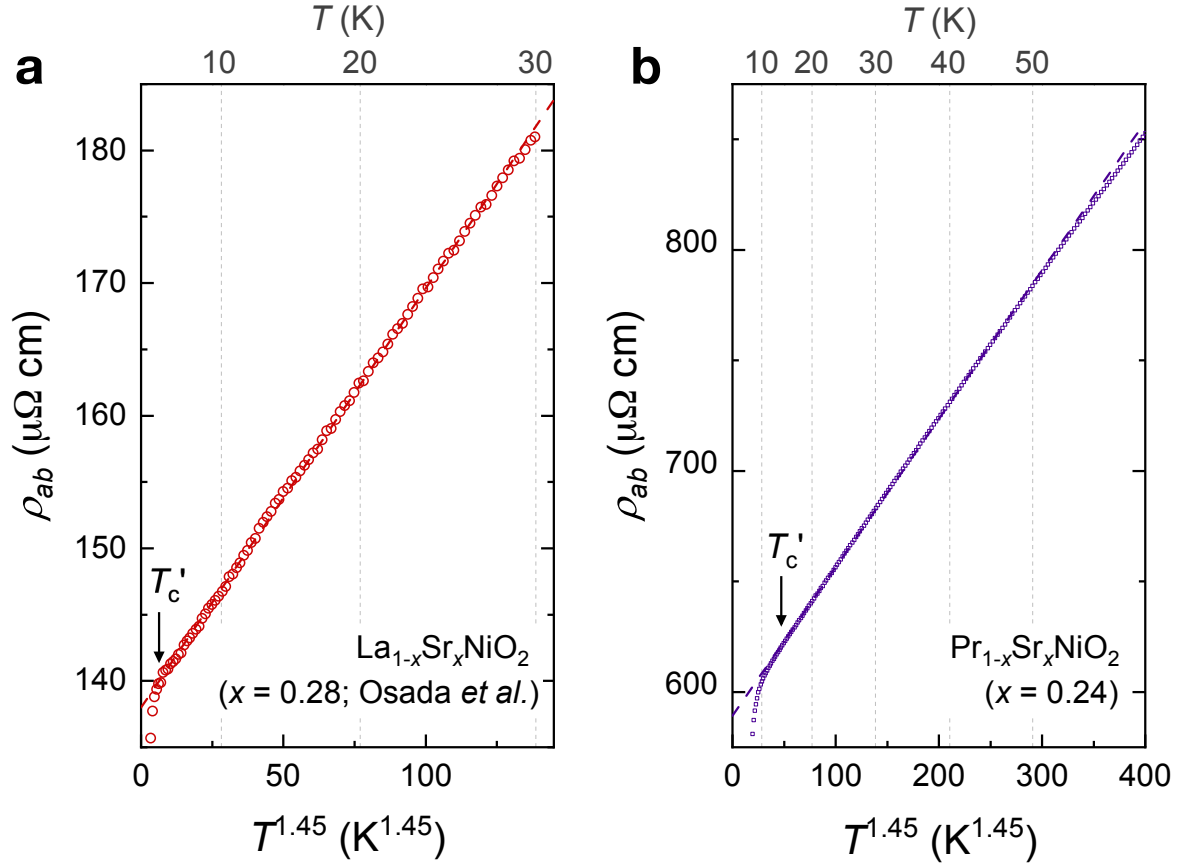
**Supplementary Figure** 13: **Power-law versus dual-component description for the low-$T$ normal-state resistivity.** **a**, A dual-component expression ($\rho(T) = \rho_0 + \alpha_1 T + \alpha_2 T^2$; blue dashed line) is used to fit the experimental $\rho_{ab}(T)$ between 3 and 18 K, within which the corresponding $\mathrm{d}\rho_{ab}/\mathrm{d}T$ (measured at 14 T) shows apparent $T$-linearity with a finite intercept. In comparison with the power-law fit ($\rho(T) = \rho_0 + \alpha_n T^n$; orange dashed-dotted line), the experimental agreement of the dual-component fit is confined within a much narrower $T$-window, making it difficult to perform any quantitative analysis of such fits. Blue dotted line corresponds to a purely $T^2$ resistivity ($\rho(T) = \rho_0 + A_2 T^2$) as $T \to 0$. (**b, c**) The same analysis applied to **b**, moderately overdoped films ($0.25 \geqslant x \geqslant 0.175$) and **c**, heavily overdoped films beyond the SC region ($x \geqslant 0.30$). For $x \leqslant 0.275$, the power-law and dual-component expressions are fitted to the same $T$-window between $3T_0$ and the highest temperature at which resistivity is measured in applied magnetic fields (34 T for $0.25 \geqslant x \geqslant 0.175$; 14 T for $x = 0.275$). For $x = 0.30$ and 0.3125, fitting 12-T data between $3T_0$ and 20 K (at which $\mathrm{d}\rho_{ab}/\mathrm{d}T$ shows a kink) finds $\alpha_1 \approx 0$, therefore the same constraint is applied to $x = 0.325$ using the dual-component description.
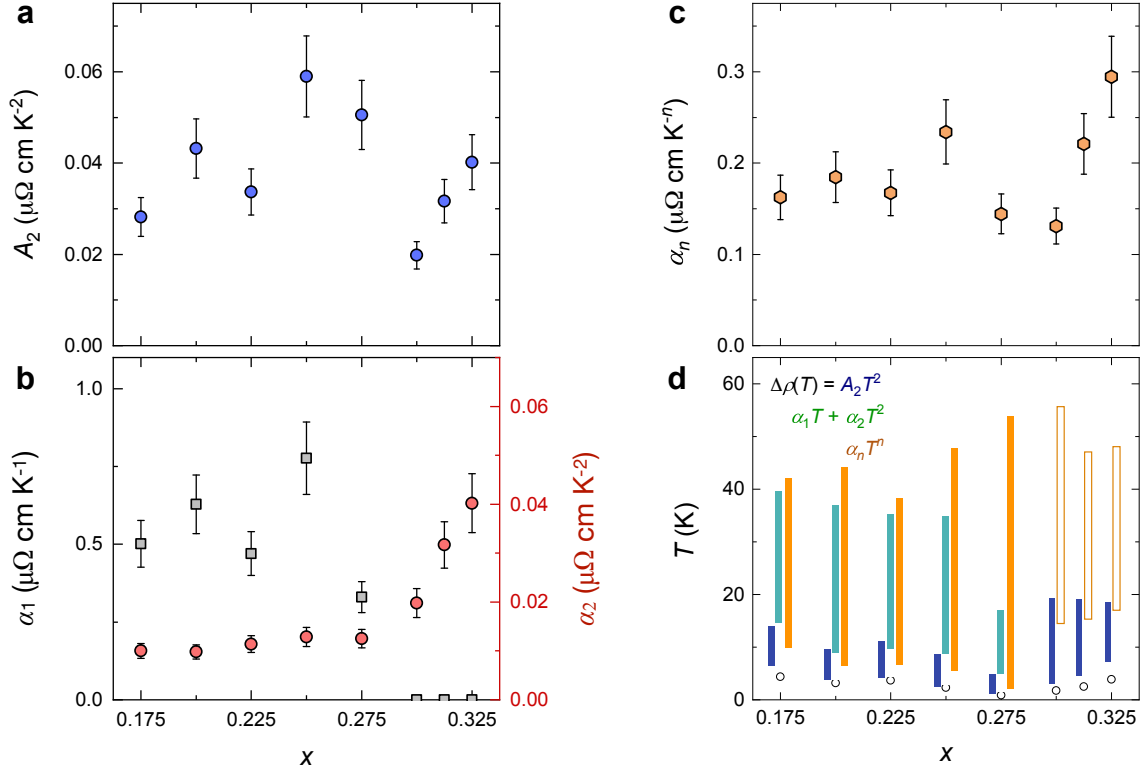
**Supplementary Figure** 14: **Doping dependence of fitting parameters and window of validity for $\rho(T)$ models considered. a**, Pure $T^2$ resistivity: $\rho(T) = \rho_0 + A_2 T^2$. **b**, Dual-component resistivity: $\rho(T) = \rho_0 + \alpha_1 T + \alpha_2 T^2$. **c**, Power-law resistivity: $\rho(T) = \rho_0 + \alpha_n T^n$. The error bars in $A_2$ and $\alpha_{1,2,n}$ correspond to the geometric uncertainties of measured samples, assumed to be 15%. **d**, Valid $T$-window for each resistivity model considered, with filled (open) bars correspond to data measured in large ($> 10$ T) and zero magnetic field, respectively. Open circles correspond to $T_0(x)$. For $x \leqslant 0.275$, the low-$T$ $T^2$ behaviour which applies only to a very narrow $T$-window is likely caused by the onset of the very low-$T$ resistive upturns; whereas for $x \geqslant 0.30$, the $T^2$ behaviour is valid over a more extended $T$-window in the $T \to 0$ limit and crossovers to $T^{1.45}$ behaviour above $\approx 20$ K.
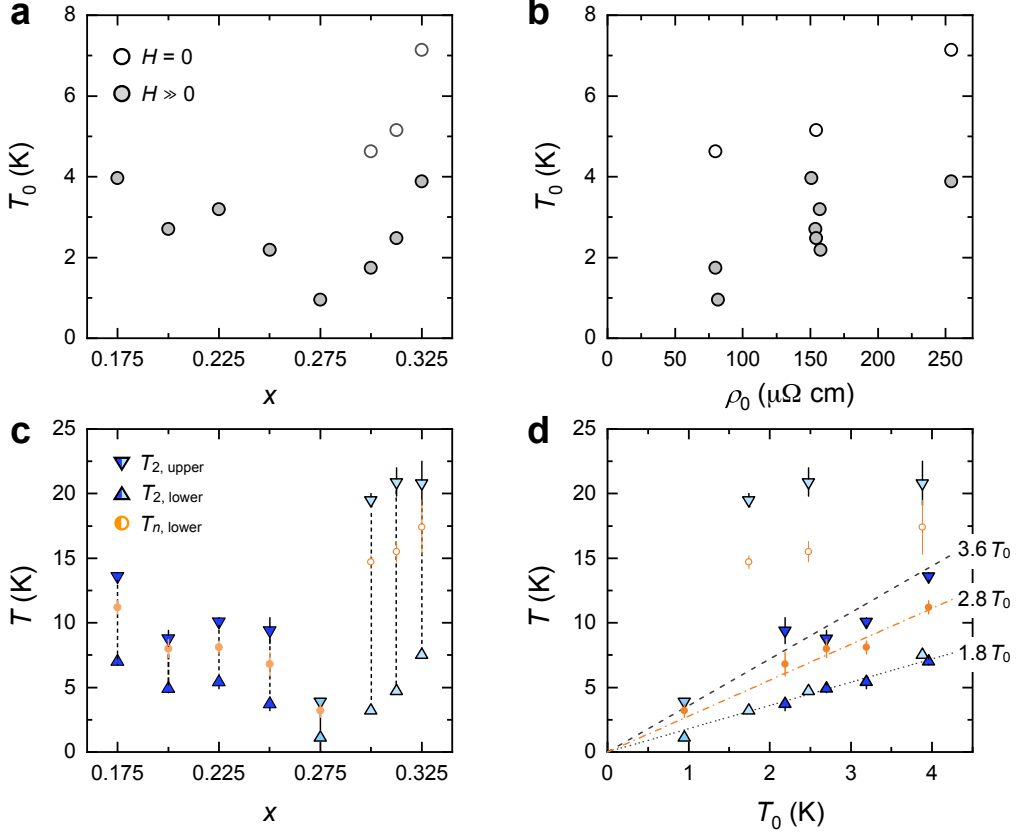
**Supplementary Figure** 15: (**a, b**) $T_0$ as a function of **a**, $x$ and **b**, $\rho_0$ for OD NSNO ($x \geqslant 0.175$). Open and filled symbols correspond to $T_0$ measured in zero and large applied magnetic fields, respectively. (**c, d**) Upper and lower bound in which $T^2$ resistivity is found ($T_{2,\text{upper}}$ and $T_{2,\text{lower}}$) and lower bound of $T^{1.45}$ resistivity, plotted against **c**, $x$ and **d**, corresponding $T_0$. Filled and open symbols correspond to temperature scales extracted from high-field measurements ($\mu_0 H = 34$, 14, and 12 T for $0.175 \leqslant x \leqslant 0.25$, $x = 0.275$, and $x \geqslant 0.30$, respectively). Error bars in $T_2$ and $T_n$ are given by the uncertainty in extracted values between the two methods defined in Supplementary Note A. For $0.175 \leqslant x \leqslant 0.275$, both $T_{2,\text{upper}}$ and $T_{2,\text{lower}}$ are found to track $T_0$ closely, suggesting the apparent $T^2$ behaviour results from the onset of resistivity upturn. In contrast, for $x \geqslant 0.30$, while $T_{2,\text{lower}}$ also tracks $T_0$, $T_{2,\text{upper}}$ extends to higher temperatures ($\approx 20$ K) and is largely uncorrelated to $T_0$, indicating the apparent $T^2$ resistivity is not caused by the resistive upturn occurring below 4 K, therefore signifying a recovery of low-$T$ $T^2$ resistivity beyond $x = 0.30$.

**Supplementary Figure** 16: $T^{1.45}$ **resistivity power law in overdoped La- and Pr-nickelate superconductors.** $\rho_{ab}$ versus $T^{1.45}$ for **a**, high-quality $La_{1-x}Sr_xNiO_2$ ($x = 0.28$; ref.[10]) and **b**, $Pr_{1-x}Sr_xNiO_2$ ($x = 0.24$; ref.[11]). An approximate linear-in-$T^{1.45}$ behaviour in $\rho_{ab}(T)$ is found between $T_c'$ and up to 50 K for both $La_{1-x}Sr_xNiO_2$ and $Pr_{1-x}Sr_xNiO_2$ beyond optimal doping.

**Supplementary Note F: Possible influence of charge/spin fluctuations on charge transport**

The convergence of the extrapolated critical doping level at which 1) the sign change in Hall coefficient $R_H(T \to 0)$, 2) the elimination of the correlation-driven resistive upturn, and 3) the most extended $T$-linear resistivity all occur, suggests that a transition of the underlying electronic ground state takes place at $x_{opt}$. Moreover, the extension of the $T$-linear resistivity down to $\lesssim 50$ K, substantially lower than the Debye temperature $\Theta_D \approx 340$ K (ref.[12]), and the marked asymmetry observed in the fan-like region of $T$-linear transport are both inconsistent with a dominant electron-phonon interaction and is more indicative of an unconventional scattering mechanism. Notwithstanding, $\rho_{ab}(T)$ in the $x = 0.1625$ film deviates markedly from perfect linearity in the (field-induced) normal state below $T_c$. This circumstance is distinct from that found in hole-doped cuprates near optimal doping e.g. LSCO,[5,13] despite the similarities in the form of $\rho_{ab}(T)$ of NSNO and LSCO above $T_c$.[2] Given the fact that the lower temperature bound of $T$-linearity in the $x = 0.1625$ film largely coincides with the upper bound of $T^{1.5}$ behaviour in the OD region, we speculate that the $T$ and $T^{1.5}$ dependence may originate from electron scattering off critical fluctuations of distinct sectors, namely charge and spin. In such a scenario, in the OD region at low $T$ where charge fluctuations are absent, current dissipation is dominated by scattering off spin fluctuations that are found to occupy much of the $T - x$ phase space.[14–17] Near $x_{opt}$, charge fluctuations could become dominant and give rise to the observed 'quantum critical fan'. The scenario of charge-fluctuation-driven criticality has recently been proposed for hole-doped cuprates.[18] Evidently, further studies are required to establish the scattering mechanism responsible for the $T$-linear resistivity in the nickelates.

# Supplementary References

[1] Barisic, N. *et al.* Universal sheet resistance and revised phase diagram of the cuprate high-temperature superconductors. *Proceedings of the National Academy of Sciences* **110**, 12235–12240 (2013).

[2] Lee, K. *et al.* Linear-in-temperature resistivity for optimally superconducting (Nd, Sr)NiO$_2$. *Nature* **619**, 288–292 (2023).

[3] Hussey, N. E. *et al.* Dichotomy in the $T$-linear resistivity in hole-doped cuprates. *Phil. Trans. R. Soc. A* **369**, 1626–1639 (2011).

[4] Varma, C. *Colloquium*: Linear in temperature resistivity and associated mysteries including high temperature superconductivity. *Rev. Mod. Phys.* **92**, 031001 (2020).

[5] Cooper, R. A. *et al.* Anomalous criticality in the electrical resistivity of La$_{2-x}$Sr$_x$CuO$_4$. *Science* **323**, 603–607 (2009).

[6] Narduzzo, A. *et al.* Violation of the isotropic mean free path approximation for overdoped La$_{2-x}$Sr$_x$CuO$_4$. *Physical Review B* **77**, 220502(R) (2008).

[7] Čulo, M. *et al.* Possible superconductivity from incoherent carriers in overdoped cuprates. *SciPost Phys.* **11**, 012 (2021).

[8] Li, D. *et al.* Superconducting dome in Nd$_{1-x}$Sr$_x$NiO$_2$ infinite layer films. *Physical Review Letters* **125**, 027001 (2020).

[9] Grissonnanche, G. *et al.* Seebeck coefficient in a nickelate superconductor: electronic dispersion in the strange metal phase. *Preprints* arXiv:2210.10987v2.

[10] Osada, M., Fujiwara, K., Nojima, T. & Tsukazaki, A. Improvement of superconducting properties in La$_{1-x}$Sr$_x$NiO$_2$ thin films by tuning topochemical reduction temperature. *Physical Review Materials* **7**, L051801 (2023).

[11] Wang, B. Y. *et al.* Effects of rare-earth magnetism on the superconducting upper critical field in infinite-layer nickelates. *Science Advances* **9**, eadf6655 (2023).

[12] Ortiz, R. A. *et al.* Magnetic correlations in infinite-layer nickelates: An experimental and theoretical multimethod study. *Physical Review Research* **4**, 023093 (2022).

[13] Giraldo-Gallo, P. *et al.* Scale-invariant magnetoresistance in a cuprate superconductor. *Science* **361**, 479–481 (2018).

14 Lu, H. *et al.* Magnetic excitations in infinite-layer nickelates. *Science* **373**, 213–216 (2021).

15 Cui, Y. *et al.* NMR evidence of antiferromagnetic spin fluctuations in $Nd_{0.85}Sr_{0.15}NiO_2$. *Chinese Physics Letters* **38**, 067401 (2021).

16 Lin, H. *et al.* Universal spin-glass behavior in bulk $LaNiO_2$, $PrNiO_2$, and $NdNiO_2$. *New Journal of Physics* **24**, 013022 (2022).

17 Fowlie, J. *et al.* Intrinsic magnetism in superconducting infinite-layer nickelates. *Nature Physics* **18**, 1043–1047 (2022).

18 Arpaia, R. *et al.* Signature of quantum criticality in cuprates by charge density fluctuations. *Nature Communications* **14**, 7198 (2023).